ADVANCED MATERIALS

Supporting Information

for *Adv. Mater.,* DOI: 10.1002/adma.202100519

Convergence of Machine Vision and Melt Electrowriting

Pawel Mieszczanek, Thomas M. Robinson, Paul D. Dalton, and Dietmar W. Hutmacher**

Supporting Information

Convergence of machine vision and melt electrowriting

P. Mieszczanek, T. M. Robinson, P. D. Dalton, D. W. Hutmacher

GitHub repository with Matlab code used in this study:
https://github.com/Lasonic/machine-vision-publication

Simulations

The process was modelled *in silico* using COMSOL Multiphysics Simulation Software (Version 5.1, COMSOL Inc., USA) to calculate the electric field. The geometries of the components of the in-house built MEW device were recreated and the electrical conductivities of the simulated objects were assigned according to properties of the physical components (stainless steel nozzle: 1.45×10^{6} [S m^{-1}]; air (at 20°C): 5×10^{-15} [S m^{-1}]; aluminium collector: 3.774×10^{-7} [S m^{-1}]) [1]. The decline of the intensity of the electrostatic forces was simulated for 4.25 kV at a distance between 4.0 and 4.9 mm [1]. Using 4.25 kV as the lowest starting HV is based on experience, as lower HV at a collector distance of 4.0 mm would not provide sufficient electrostatic force to generate homogeneous fibres. Along the increasing distance, the simulation further included a simultaneously growing scaffold (1000 µm pore size, 17,5 µm fibre width) with an assumed electrical conductivity of 10×10^{-10} [S m^{-1}], which is typical for molten polymers [2].

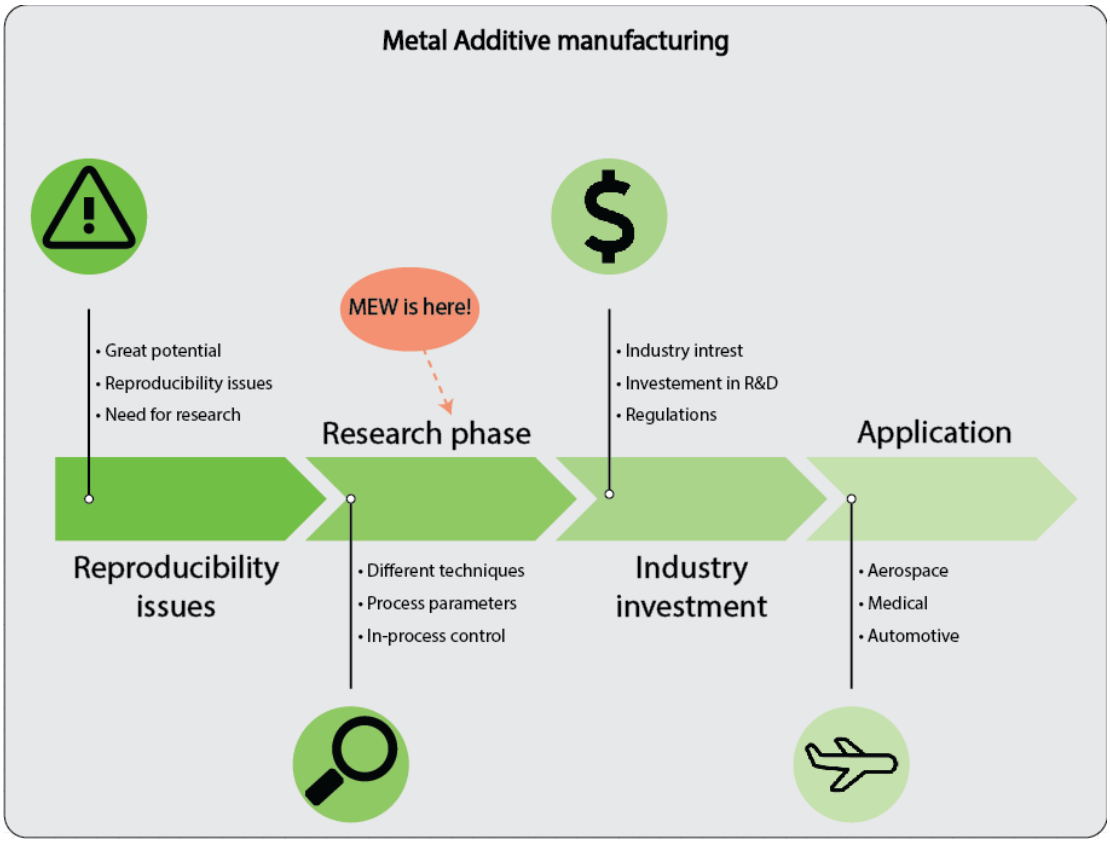

Supporting Figure S1. MEW in context of metal-based AM development. Currently, the technology is in the research phase, which focuses on the development of the first closed-loop control of the MEW printing process.

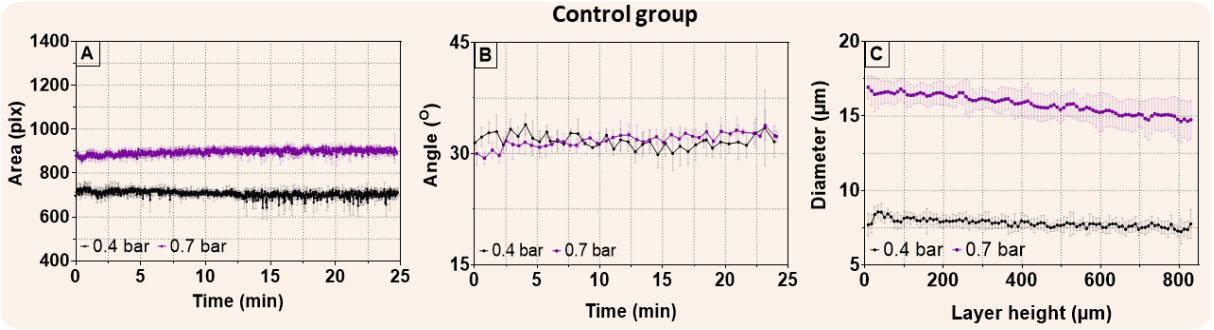

Supporting Figure S2. **(A)** Taylor cone size, **(B)** jet angle and **(C)** fibre diameter of the control electric field where high voltage and working distance remain unchanged throughout the print. The results suggest stable printing conditions except fibre diameter at 0.7 bar which decreases with the layer count.

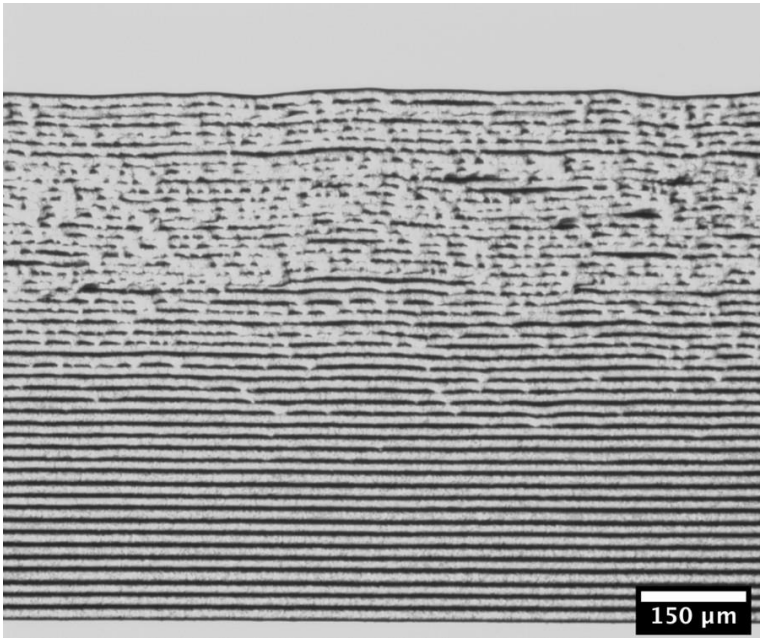

Supporting Figure S3. SEM image example of extensive fibre fusing caused by the heat radiating from the printed at close distance to the sample. Therefore, for printing of high structures it is necessary to incrementally increase working distance with each layer to maintain fibre stacking and avoid fibre fusion.

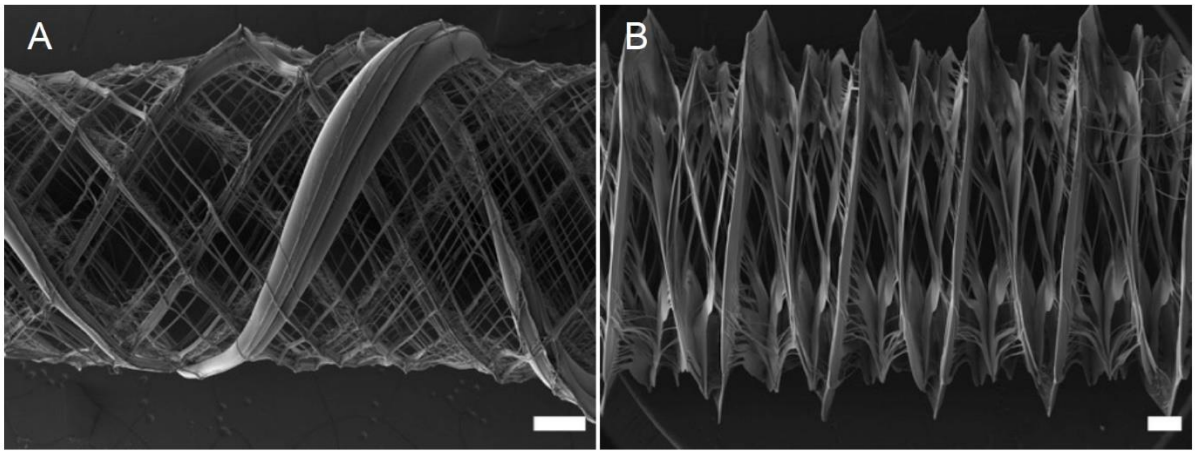

Supporting Figure S4. Two potential defects during the fabrication of thick MEW tubes. These include (A) fibre pulsing and (B) fibre bridging, when fibre stacking is disrupted due to the attraction/repulsion from neighbouring fibres [3]. Both scale bars are 500 µm.

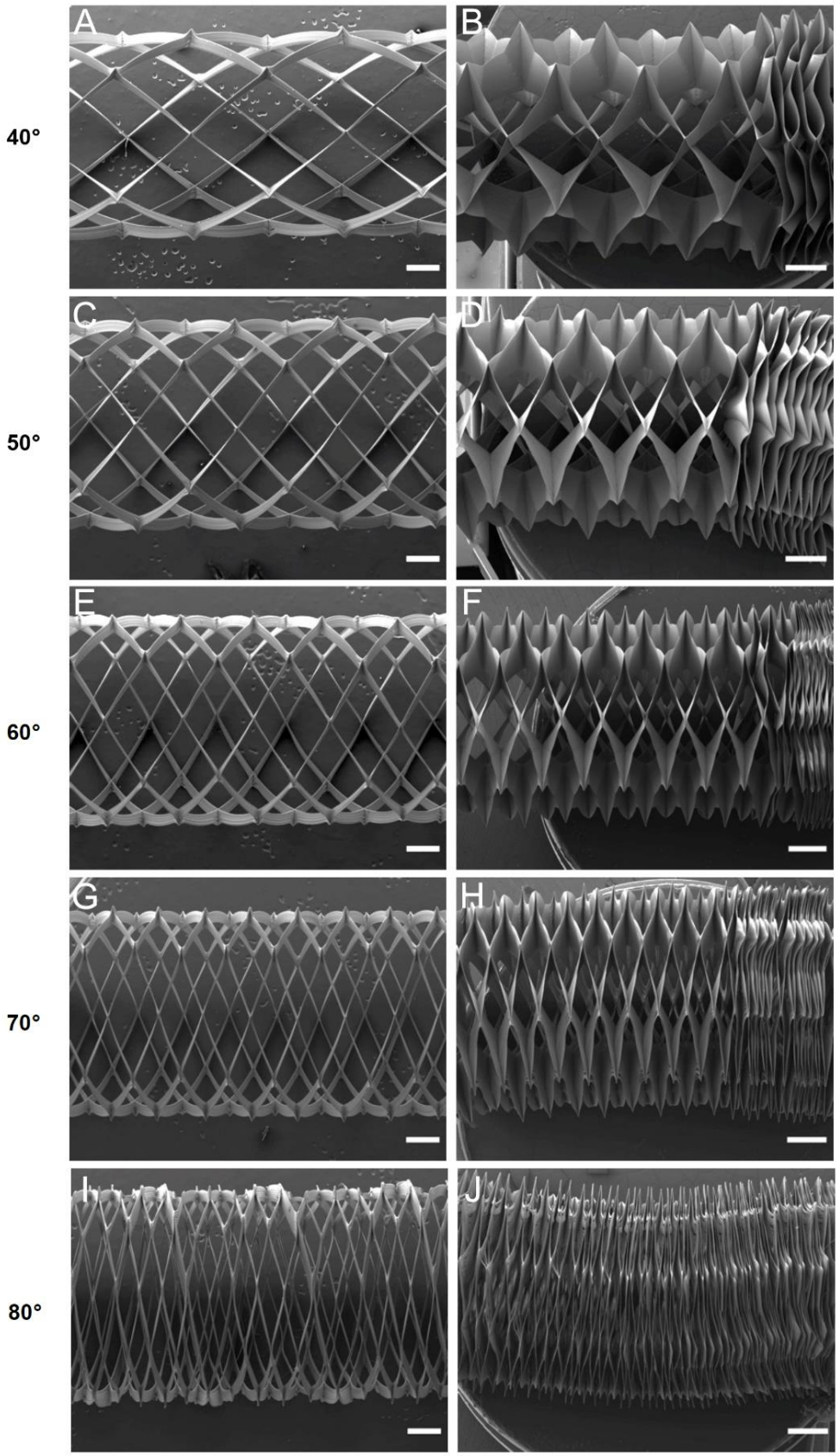

Supporting Figure S5. Comparison of all melt electrowritten tubes with different WA and constant PP. The desired WA was shown for (A) 40°, (C) 50°, (E) 60°, (G) 70° and (I) 80° at 10 layers. Partially compressed tube ends are demonstrated for (B) 40°, (D) 50°, (F) 60°, (H) 70° and (J) 80° at 80 layers. All scale bars for (A), (C), (E), (G) and (I) are 500 μm, and (B), (D), (F), (H) and (J) are 1 mm, respectively.

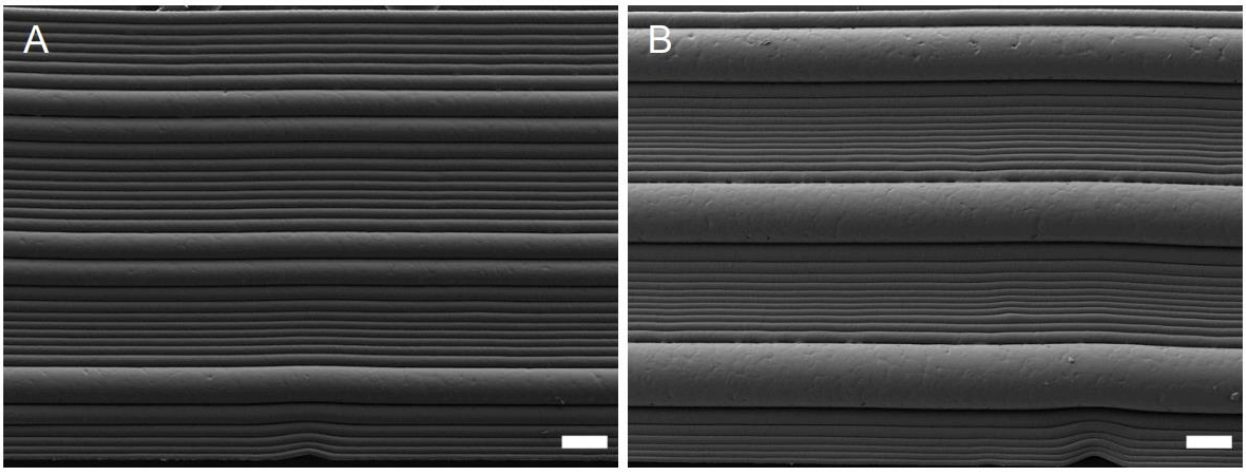

Supporting Figure S6. Examples of fibre pulsing along the z-axis, occurring within the first 50 layers. Both (A) and (B) were fabricated by printing along the length of the mandrel without rotation with a starting applied voltage of 4.25 kV and a collector distance of 4.0 mm using a constant electric field. All scale bars are 50µm.

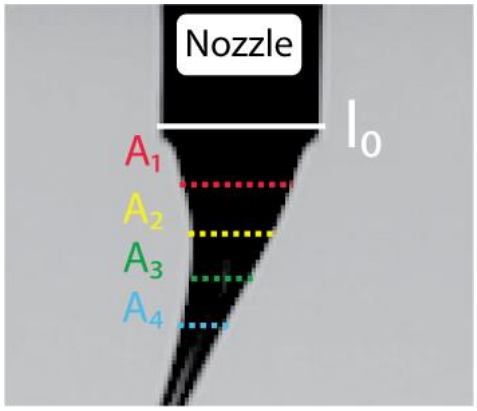

Supporting Figure S7. Since the boundary between Taylor cone and fibre jet is unclear, Taylor cone was computed at 4 different regions (A_1, A_2, A_3 and A_4) each starting from the line l_0 defined by the end of the nozzle.

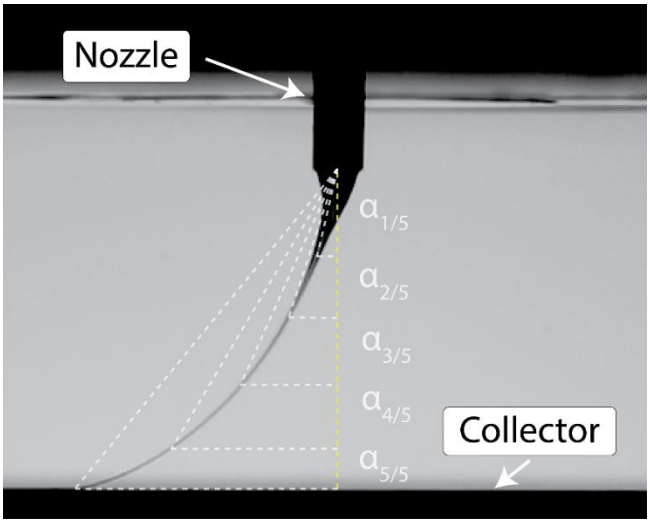

Supporting Figure S8. Jet angle was computed at 5 different locations ($\alpha_{1/5}$ etc.) along the jet to identify the ideal jet angle measurement point. Each angle was computed from the tip of the nozzle.

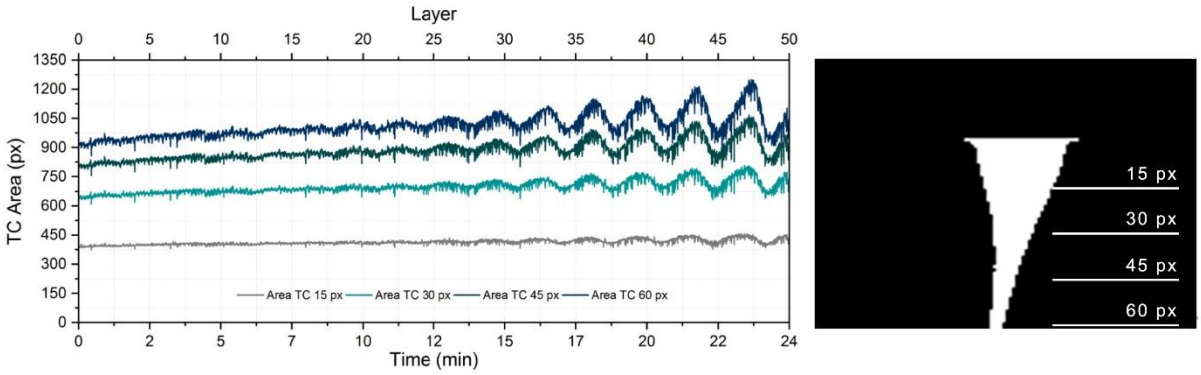

Supporting Figure S9. Example of a plot showing Taylor cone area measurement during pulsing at 4 different regions described in the right-hand side segmentation. An area of 60 px from the nozzle was selected for analysis in this study as it clearly captures even small changes of Taylor cone area as well as provides the best measurement resolution of the occurring changes. Right hand side image is an example of Taylor cone segmentation performed using developed MATLAB algorithm. White pixels represent the detected Taylor cone area.

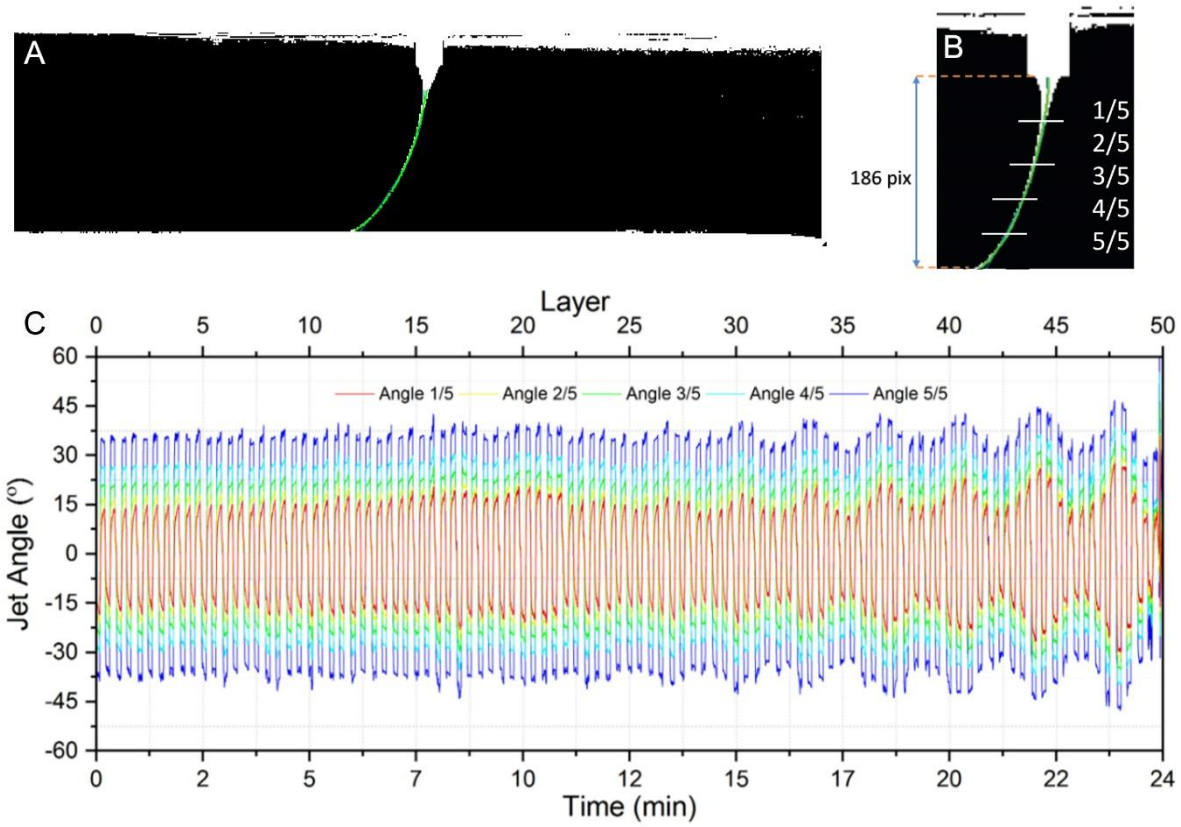

Supporting Figure S10. Example of fibre jet segmentation and tracking performed using developed MATLAB algorithm. (A, B) Green pixels represent detected fibre jet. (C) Example of a plot showing jet angle measurement

during pulsing at 5 different points long the fibre jet described in Supporting Figure S7. Angle 4/5 was selected for analysis in this study as it is less vulnerable to measurement error ~~in comparison with Angle 5/5~~.

References

1. Wunner, F. M.; Wille, M. L.; Noonan, T. G.; Bas, O.; Dalton, P. D.; De-Juan-Pardo, E. M.; Hutmacher, D. W., *Adv Mater* **2018,** *30* (20), e1706570. DOI 10.1002/adma.201706570.
2. Zhmayev, E.; Zhou, H.; Joo, Y. L., *Journal of Non-Newtonian Fluid Mechanics* **2008,** *153* (2-3), 95-108. DOI 10.1016/j.jnnfm.2007.11.011.
3. Kim, J.; Bakirci, E.; O'Neill, K. L.; Hrynevich, A.; Dalton, P. D., *Macromolecular Materials and Engineering n/a* (n/a), 2000685. DOI 10.1002/mame.202000685.